A Compact 8×8 Dual-Band MIMO Antenna Array with Hybrid Decoupling for Sub-6 GHz and mmWave 5G Smartphone Terminals

Adnane Ghiat[1,*], *Jesús R.* Pérez[2,**], *Abdelwahed* Tribak[1], *Jaouad* Terhzaz[3], and *Rafael* P. Torres[2]

[1]Department of Microwave and Communication, INPT, Rabat, Morocco
[2]Department of Communications Engineering, Universidad de Cantabria, Santander, Spain
[3]Département de Physique, CRMEF Casablanca-Settat, Casablanca, Morocco

Abstract. A compact dual-band Multiple-Input Multiple-Output (MIMO) antenna array comprising eight elements is reported for deployment in 5G handheld terminals. The array simultaneously addresses the n78 band (3.4–3.8 GHz) and the n258 millimeter-wave band (24.5–27.5 GHz), realizing both operating ranges within a single-layer substrate whose overall dimensions are compatible with contemporary smartphone form factors. Each radiating element combines a T-shaped primary branch with two asymmetric C-shaped resonators, a topology that produces independent resonances at the two target bands. Inter-element isolation is enhanced through the joint action of defected ground structures (DGS) and a passive neutralization line (NL), which together raise the minimum isolation from approximately 11 dB to 18 dB across the full bandwidth. Cross-validation by CST Microwave Studio and ANSYS HFSS confirms realized gains of 5.7 dBi at 3.6 GHz and 6.4 dBi at 26 GHz, total radiation efficiency in the 85–94 % range, and envelope correlation coefficients (ECC) below 0.04—all confirming suitability for spatial-multiplexing operation in next-generation mobile devices.

1 Introduction

Fifth-generation (5G) cellular technology requires a fundamental re-architecture of mobile networks, driven by demands for gigabit-class throughputs, sub-millisecond round-trip latency, and the capacity to serve densely packed device populations. These service classes are formally expressed as enhanced mobile broadband (eMBB), ultra-reliable low-latency communication (URLLC), and massive machine-type communication (mMTC) [1]. Realizing such capabilities at the terminal side depends critically on multiple-input multiple-output (MIMO) antenna systems, which exploit spatial degrees of freedom to multiply channel capacity without additional spectrum [2].

Two distinct spectral regions are exploited by 5G deployments. The sub-6 GHz tier—in particular the 3.4–3.8 GHz band (n78) allocated in many national frameworks—provides wide-area coverage and reasonable building-penetration characteristics. By contrast, millimeter-wave allocations such as 24.5–27.5 GHz (n258) support extreme data rates

*e-mail: adnane.ghiat@inpt.ac.ma
**e-mail: jesus.perez@unican.es

at the cost of reduced propagation range and heightened sensitivity to blockage [2, 3]. Designing a single antenna assembly that operates efficiently across both tiers imposes conflicting requirements: the physical aperture that governs gain at sub-6 GHz would occupy an impractical fraction of the handset area at millimeter-wave frequencies, while the tight tolerances needed for millimeter-wave performance must coexist with the wider, more forgiving geometry of the sub-6 GHz element.

Researchers have addressed these tensions through several families of techniques. At sub-6 GHz, defected ground structures (DGS) are widely used to suppress surface-wave propagation and thereby improve isolation between adjacent elements [4]; characteristic mode analysis guides the identification of well-separated orthogonal modes suitable for MIMO operation [5]; and slot-loading of patch radiators widens impedance bandwidth while providing additional degrees of freedom for isolation control [6]. At millimeter-wave frequencies, stub-loaded coplanar waveguide feeds [7], metamaterial-inspired periodic structures [8], and orthogonally polarized element pairs [9] have demonstrated effective mutual coupling suppression even at sub-millimeter spacings.

The metric landscape reported in recent literature is encouraging: ECC values below 0.05 [10], port isolation exceeding 20 dB [11], and radiation efficiencies above 85 % [12] have all been demonstrated. Further refinements include circular-polarization schemes [13], electromagnetic bandgap (EBG) integration [14], PIN-diode reconfigurability , and parasitic-element miniaturization [15]. Despite this progress, the simultaneous satisfaction of compactness, dual-band coverage, high isolation, and low ECC within a smartphone-scale substrate remains a design challenge of practical significance.

The present work tackles this challenge by combining a frequency-optimized composite radiator with a hybrid decoupling strategy consisting of DGS slots and a printed neutralization line. The following sections describe the element and array geometry, analyze the isolation mechanisms, and present simulated gain, efficiency, and diversity metrics that collectively validate the design for 5G handset integration.

2 Proposed Antenna Architecture

2.1 Element Geometry and Substrate Selection

Figure 1 and Table 1 describe the layout of the eight-element array and the optimized dimensional values of each constituent element. The entire structure is implemented on a single metallization layer of Rogers RO4003C laminate, whose relative permittivity of $\varepsilon_r = 3.5$ and dissipation factor of $\tan\delta = 0.0027$ represent a well-characterized combination for microwave and millimeter-wave co-design. The substrate measures $140 \times 70 \times 0.5\,\text{mm}^3$, a footprint consistent with mainstream smartphone dimensions.

The ground plane spans the full substrate area but incorporates clearance slots of width G_x along the lateral edges and G_y along the horizontal edges. A cross-shaped aperture at the substrate center serves a dual purpose: it promotes edge-mode radiation for the sub-6 GHz elements and acts as a first-level coupling barrier between element pairs located on opposite sides of the device.

Each radiating element occupies a $14 \times 9.8\,\text{mm}^2$ footprint. The primary radiator is a T-shaped metallic branch fed by a $50\,\Omega$ microstrip line of width W_f and length L_f. Two C-shaped parasitic resonators are attached asymmetrically to the lateral extremities of the T-branch: the left resonator is defined by parameters $(W_{b1}, L_{b1}, W_{a1}, L_{a1})$ and the right resonator by $(W_{b2}, L_{b2}, W_{a2}, L_{a2})$. The deliberate dimensional asymmetry between the two C-sections is central to the dual-band mechanism, as described in Section 2.2. Each element is excited through a 50 Ω SMA connector soldered through a via on the substrate reverse side, isolating the feed network from the radiating aperture.

Table 1. Optimized dimensional parameters of the antenna element.

Parameter	Value (mm)
W_f	0.8
L_f	6.0
W_t	13.5
W_{b1}	0.4
L_{b1}	1.6
W_{a1}	4.5
L_{a1}	0.4
W_{b2}	0.1
L_{b2}	3.8
W_{a2}	9.0
L_{a2}	0.6
G_x	6.0
G_y	5.4
S	8.0

2.2 Dual-Band Resonance Mechanism

To elucidate the contribution of each geometric stage to the final dual-band response, a four-step design progression was carried out on an isolated element; the $|S_{11}|$ trace for each stage is shown in Figure 2.

Stage 1. The isolated T-branch (without any C-section) produces a broadband single resonance near 17 GHz with a bandwidth exceeding 10 GHz. This initial response demonstrates adequate energy coupling to the T-aperture but provides no frequency selectivity between the sub-6 GHz and millimeter-wave targets.

Stage 2. Attaching an inverted-L stub to the right boundary of the T-branch creates the first C-shaped path. This addition perturbs the current distribution sufficiently to split the single-band response into two resonances near 14 GHz and 23 GHz, establishing the dual-band character of the element. Neither resonance is yet aligned with the 5G allocations of interest.

Stage 3. A second inverted-L stub, geometrically distinct from the first, is appended to the left boundary of the T-branch, completing the asymmetric dual-C topology. The intentional dimensional inequality between the two C-sections allows independent control of the two resonant frequencies, which shift toward the target bands but remain slightly misaligned at this stage.

Stage 4 (Finalized design). Fine-tuning of the segment lengths and widths relocates both resonances precisely within the n78 band (3.4–3.8 GHz) and the n258 band (24.5–27.5 GHz), confirming that the asymmetric C-section topology is an effective mechanism for independently steering sub-6 GHz and millimeter-wave resonances.

https://doi.org/10.1051/epjconf/202638001005

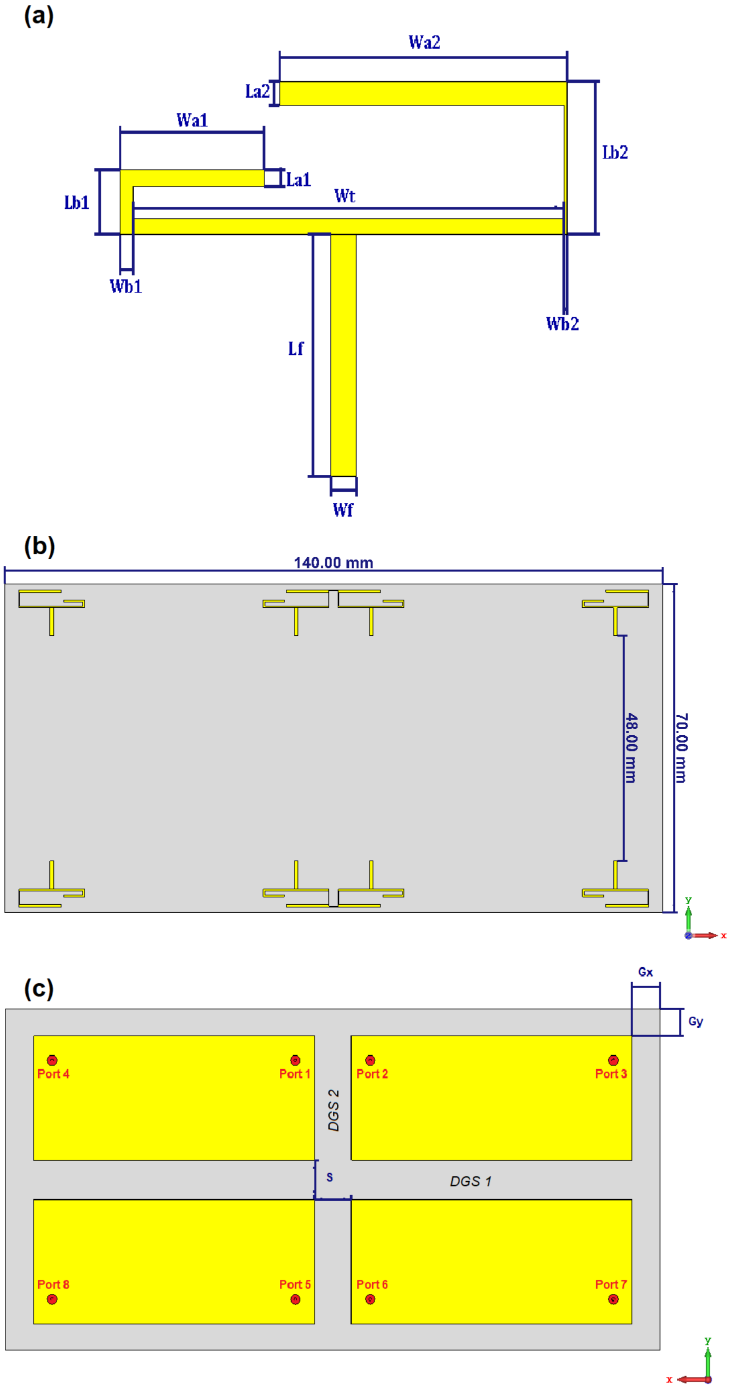

Figure 1. Geometry of the dual-band eight-element MIMO array. (a) Single radiating element. (b) Array top view. (c) Ground-plane back view.

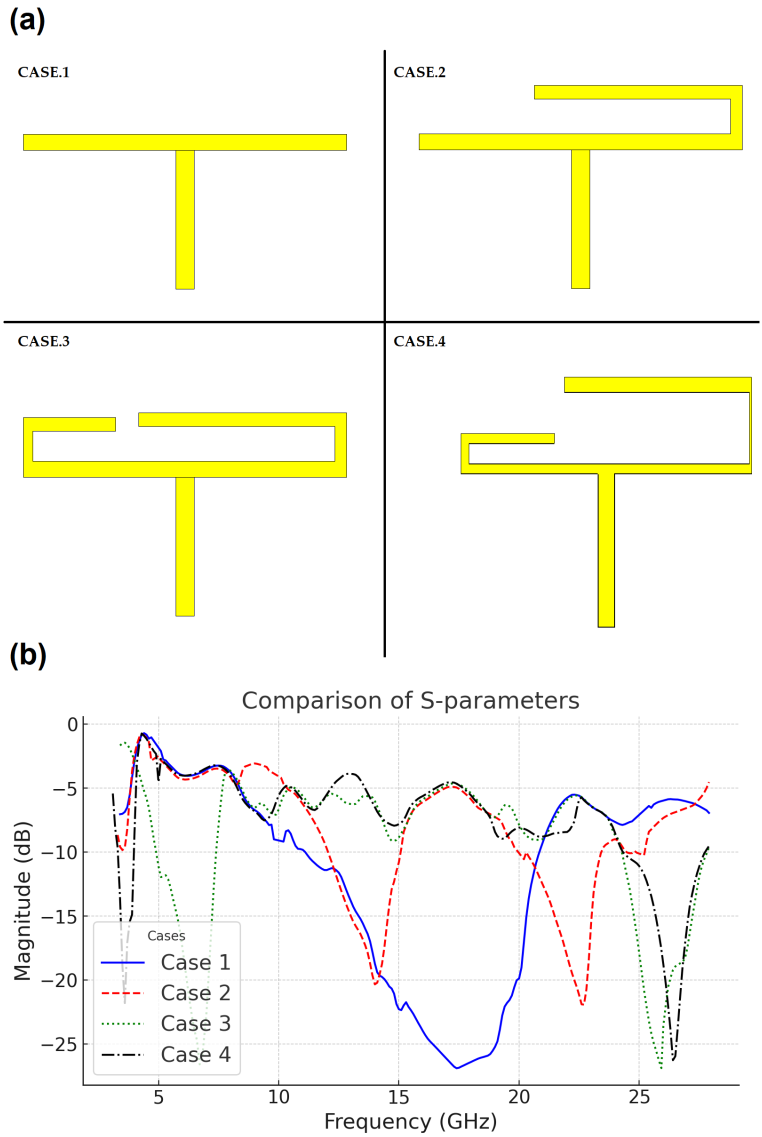

Figure 2. (a) Sequential design stages of a single antenna element. (b) Corresponding simulated reflection coefficients.

3 Eight-Element Array Performance

3.1 Impedance Matching

The eight antenna elements are symmetrically distributed about the substrate center line, with an edge-to-edge spacing of 48 mm between opposing element pairs. This arrangement balances compactness against the isolation requirement inherent to MIMO operation. Figure 3 shows the simulated reflection coefficients obtained independently with CST Microwave Studio and ANSYS HFSS; the close agreement between the two solvers validates the simulation

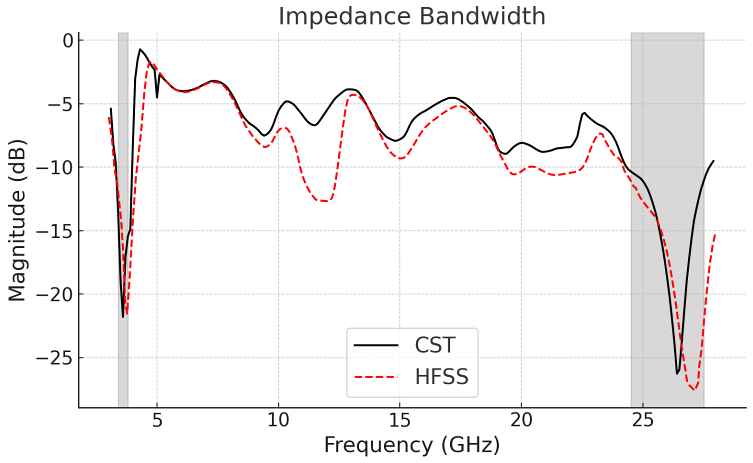

Figure 3. Simulated $|S_{11}|$ for each port of the eight-element MIMO array, confirming dual-band coverage of the n78 and n258 allocations.

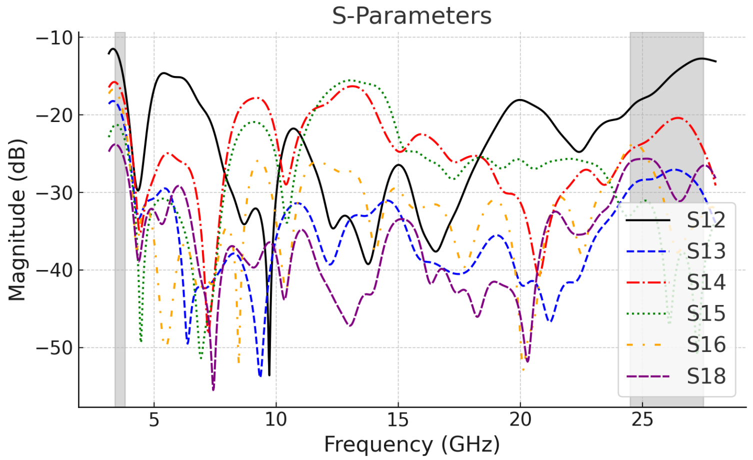

Figure 4. Simulated mutual coupling $|S_{ij}|$ between all port combinations of the eight-element array.

methodology and confirms full coverage of both the n78 (3.4–3.8 GHz) and n258 (24.5–27.5 GHz) bands for all array ports.

3.2 Mutual Coupling and Hybrid Decoupling

Mutual coupling between proximate elements is the principal factor that limits MIMO channel capacity in compact arrays. The transmission coefficients S_{ij} ($i \neq j$) plotted in Figure 4 reveal that most element pairs maintain isolation well above the 15 dB threshold commonly cited in the literature. An exception arises at the center of each substrate edge, where ports 1 and 2 (and symmetrically ports 4 and 5) are separated by only 16 mm; at this reduced spacing the coupling rises to approximately 11 dB, insufficient for reliable MIMO operation.

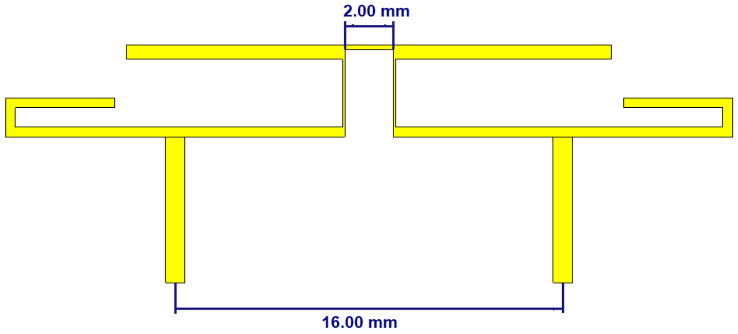

Figure 5. Printed neutralization line (NL) connecting the closely spaced center port pair.

To remedy this, two complementary passive countermeasures are incorporated, as illustrated in Figure 5. First, a printed neutralization line (NL) is routed between the closely spaced center elements. The NL introduces an auxiliary signal path whose phase and amplitude are tuned to cancel the dominant coupling current, suppressing surface-wave leakage between the affected ports across the full operational bandwidth. Second, a pair of defected ground structures (DGS) are etched into the ground plane at the locations of highest current density. The DGS apertures interrupt the surface-current return paths that sustain coupling at millimeter-wave frequencies, where the skin depth is particularly shallow and surface waves are most pronounced.

The quantitative impact of these structures is assessed in Figure 6. Introduction of the DGS alone raises the isolation at the critical port pair by approximately 3 dB in the millimeter-wave band. Activating the NL in addition provides further broadband decoupling, bringing the combined improvement to approximately 7 dB and elevating the minimum isolation across the entire array to about 18 dB—a value consistent with the requirements of spatial-multiplexing MIMO.

3.3 Gain, Efficiency, and Diversity Metrics

Figure 7 presents the realized gain and total radiation efficiency as functions of frequency. Peak gains of 5.7 dBi at 3.6 GHz and 6.4 dBi at 26 GHz are achieved, figures that are competitive with the single-layer designs reported in the recent literature for analogous dual-band applications. The total radiation efficiency remains within the 85–94 % range across both operating bands, confirming that ohmic and mismatch losses are well controlled in the optimized geometry.

The envelope correlation coefficient quantifies the statistical independence of the signals received by distinct antenna elements, a prerequisite for effective spatial multiplexing. ECC values derived from the complex far-field patterns of all element pairs are shown in Figure 8; they remain below 0.04 throughout both bands. This low correlation confirms that the array produces sufficiently orthogonal radiation patterns, enabling the spatial multiplexing gain predicted by information-theoretic analysis of MIMO channels.

4 Conclusion

A dual-band 8×8 MIMO antenna array has been designed and characterized for integration into 5G smartphone terminals. The radiating element, consisting of a T-shaped branch

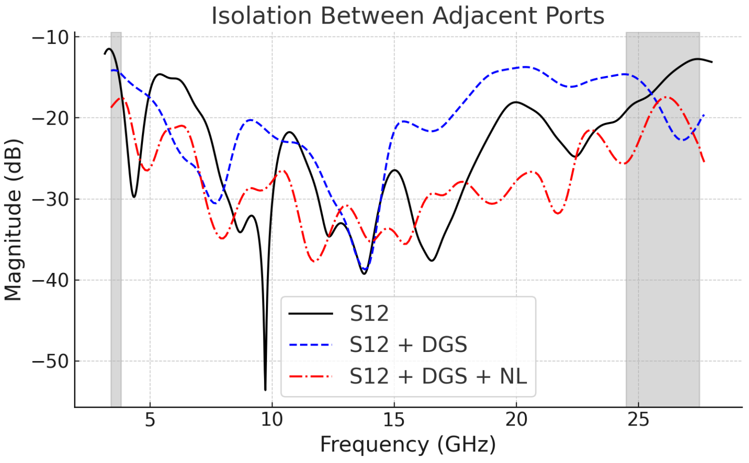

Figure 6. Progressive isolation improvement at the center element pair: reference (no treatment), after DGS only, and after DGS + NL.

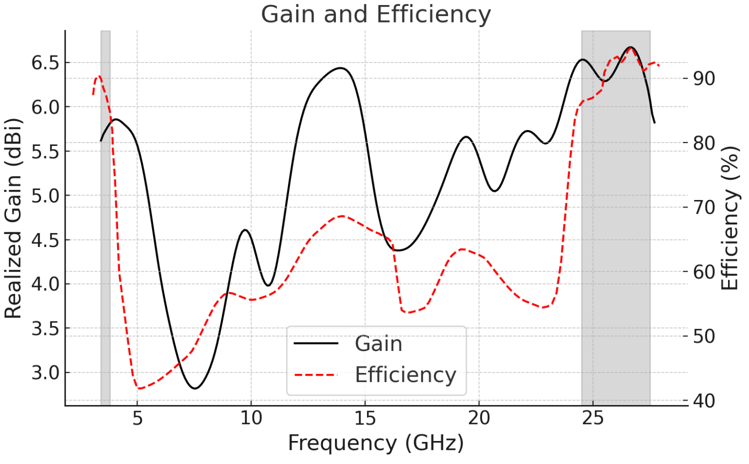

Figure 7. Realized gain (left axis) and total radiation efficiency (right axis) over the dual operating bands.

flanked by two geometrically asymmetric C-shaped resonators on a Rogers RO4003C substrate, achieves independent dual-band coverage of the n78 (3.4–3.8 GHz) and n258 (24.5–27.5 GHz) allocations within a footprint of only $14 \times 9.8\,\text{mm}^2$. A hybrid decoupling strategy combining defected ground structures and a printed neutralization line raises the minimum inter-element isolation from 11 dB to 18 dB, addressing the pronounced coupling observed at the 16 mm separation of the center element pair. Dual-solver validation with CST and HFSS confirms realized gains of 5.7 dBi and 6.4 dBi, radiation efficiencies of 85–94 %, and ECC values below 0.04, collectively meeting the performance requirements for compact MIMO operation. Fabrication and integration of the array into a wideband channel sounder system

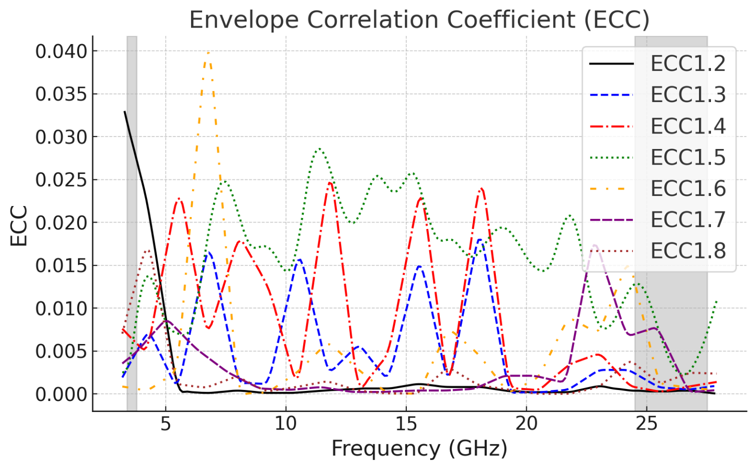

Figure 8. Envelope correlation coefficients (ECC) for all port pairs of the proposed eight-element MIMO array.

are planned as the next steps, with the goal of enabling more accurate experimental characterization of real-world 5G propagation channels.

Acknowledgements

This work has been supported by the Spanish Government under the grant PID2024-158965OB-C22 funded by MICIU/AEI/10.13039/501100011033

References

[1] K. Wu, W. Ni, T. Su, R. P. Liu, and Y. J. Guo, "5G network user experience," *IEEE Netw.*, vol. 33, no. 5, pp. 134–140, 2019. https://doi.org/10.1109/MNET.2019.1800288

[2] R. K. Raj and A. Verma, "Advances in MIMO antenna design for sub-6 GHz and mmWave 5G handsets," *IEEE Access*, vol. 11, pp. 1–30, 2023.

[3] S. A. Imam *et al.*, "Frequency planning and antenna challenges for dual-band 5G terminals," *Int. J. Electron. Commun.*, vol. 165, 154659, 2023.

[4] S. Ghosh and P. Mandal, "Design of DGS-loaded MIMO antenna with enhanced isolation for 5G applications," *AEU—Int. J. Electron. Commun.*, vol. 168, 154700, 2023.

[5] Y. Chen and C.-F. Wang, *Characteristic Modes: Theory and Applications in Antenna Engineering*. Wiley, Hoboken, NJ, 2015.

[6] A. Pant *et al.*, "Slot-loaded wideband MIMO antenna with improved port isolation," *Prog. Electromagn. Res. C*, vol. 131, pp. 123–135, 2023.

[7] M. Elnady *et al.*, "Periodically stub-loaded CPW antenna for millimeter-wave 5G handsets," *Microw. Opt. Technol. Lett.*, vol. 64, no. 8, pp. 1545–1553, 2022.

[8] A. Ramos *et al.*, "Review of metamaterial-inspired MIMO antennas for 5G mobile devices," *Sensors*, vol. 23, no. 4, 1865, 2023.

[9] A. El-Abd *et al.*, "Isolation enhancement in orthogonally oriented mmWave MIMO arrays," *IEEE Antennas Wirel. Propag. Lett.*, vol. 23, no. 2, pp. 567–571, 2024.

[10] A. Ghiat *et al.*, "Multiple-notch MIMO antenna with ECC below 0.05 for sub-6 GHz 5G," *IEEE Trans. Antennas Propag.*, 2025, in press.

[11] P. Kumar *et al.*, "Two-port MIMO antenna with greater than 20 dB isolation for 5G NR," *Int. J. RF Microw. Comput.-Aided Eng.*, vol. 33, e23605, 2023.

[12] A. Ghiat *et al.*, "Triple-band MIMO antenna with over 85 % efficiency for 5G smartphones," *Prog. Electromagn. Res. M*, vol. 127, pp. 45–57, 2024.

[13] S. Moharana *et al.*, "Circularly polarized MIMO antenna for sub-6 GHz 5G terminals," *IEEE Antennas Wirel. Propag. Lett.*, vol. 23, no. 1, pp. 234–238, 2024.

[14] S. Arulmurugan *et al.*, "Screen-printed EBG-integrated MIMO antenna for 5G handsets," *Micromachines*, vol. 15, no. 3, 412, 2024.

[15] K. S. Babu *et al.*, "Compact MIMO antenna miniaturised with parasitic strips for 5G NR," *IET Microw. Antennas Propag.*, vol. 16, no. 14, pp. 883–893, 2022.